ADVANCES IN ATMOSPHERIC SCIENCES, VOL. 33, JANUARY 2016, 21–33

Dynamic and Thermodynamic Features of Low and Middle Clouds Derived from Atmospheric Radiation Measurement Program Mobile Facility Radiosonde Data at Shouxian, China

Jinqiang ZHANG[1,2], Hongbin CHEN[*1,2], Xiang'ao XIA[1,2], and Wei-Chyung WANG[3]

[1]*Key Laboratory of Middle Atmosphere and Global Environment Observation, Institute of Atmospheric Physics, Chinese Academy of Sciences, Beijing* 100029

[2]*Collaborative Innovation Center on Forecast and Evaluation of Meteorological Disasters, Nanjing University of Information Science & Technology, Nanjing* 210044

[3]*Atmospheric Sciences Research Center, University at Albany, State University of New York, USA*

(Received 24 January 2015; revised 8 April 2015; accepted 16 June 2015)

ABSTRACT

By using the radiosonde measurements collected at Shouxian, China, we examined the dynamics and thermodynamics of single- and two-layer clouds formed at low and middle levels. The analyses indicated that the horizontal wind speed above the cloud layers was higher than those within and below cloud layers. The maximum balloon ascent speed (5.3 m s^{-1}) was located in the vicinity of the layer with the maximum cloud occurrence frequency (24.4%), indicating an upward motion (0.1–0.16 m s^{-1}). The average thickness, magnitude and gradient of the temperature inversion layer above single-layer clouds were 117 ± 94 m, $1.3 \pm 1.3^{\circ}$C and $1.4 \pm 1.5^{\circ}$C $(100\ \text{m})^{-1}$, respectively. The average temperature inversion magnitude was the same (1.3°C) for single-low and single-middle clouds; however, a larger gradient [$1.7 \pm 1.8^{\circ}$C $(100\ \text{m})^{-1}$] and smaller thickness (94 ± 67 m) were detected above single-low clouds relative to those above single-middle clouds [$0.9 \pm 0.7^{\circ}$C $(100\ \text{m})^{-1}$ and 157 ± 120 m]. For the two-layer cloud, the temperature inversion parameters were 106 ± 59 m, $1.0 \pm 0.9^{\circ}$C and $1.0 \pm 1.0^{\circ}$C $(100\ \text{m})^{-1}$ above the upper-layer cloud and 82 ± 60 m, $0.6 \pm 0.9^{\circ}$C and $0.7 \pm 0.6^{\circ}$C $(100\ \text{m})^{-1}$ above the low-layer cloud. Absolute differences between the cloud-base height (cloud-top height) and the lifting condensation level (equilibrium level) were less than 0.5 km for 66.4% (36.8%) of the cases analyzed in summer.

Key words: radiosonde, cloud, dynamics, thermodynamics

Citation: Zhang, J. Q., H. B. Chen, X. A. Xia, and W.-C. Wang, 2016: Dynamic and thermodynamic features of low and middle clouds derived from Atmospheric Radiation Measurement Program mobile facility radiosonde data at Shouxian, China. *Adv. Atmos. Sci.*, **33**(1), 21–33, doi: 10.1007/s00376-015-5032-8.

1. Introduction

Clouds affect the radiation budget of the Earth's atmosphere mainly through reflecting the incoming solar radiation, absorbing the upwelling infrared radiation, and then re-emitting it at local temperatures (Trenberth et al., 2009). Therefore, the radiative heating/cooling caused by cloud vertical distribution of single- or multi-layered clouds couple strongly with atmospheric dynamics, thermodynamics and the hydrological cycle (Del Genio et al., 2005; Kalesse and Kollias, 2013; Kunnen et al., 2013). Despite their significance, representation of clouds in global climate models is far from realistic due to inadequate understanding of the underlying dynamic and physical processes (Stephens, 2005; Tao et al., 2012) and considerable variations in cloud amount in both the vertical and horizontal directions (Zhang et al., 2005; Xi et al., 2010). The cloud feedback effects associated with climate changes have also been recognized as introducing the largest uncertainty in using models to project future climate changes (IPCC, 2007, 2013).

Sherwood et al. (2014) highlighted the importance of low clouds and the associated feedbacks in affecting climate sensitivity. Compared to low and high clouds, less attention is paid to mid-level clouds because they do not produce significant amounts of rain or snow (Sassen and Wang, 2012). However, mid-level clouds impact both the energy budget and vertical profile of heating in the atmosphere. In addition, the effects of radiative and latent heating of mid-level clouds are highly uncertain due to a lack of information about both their frequency and phase (Riihimaki et al., 2012).

Extensive surface stations, such as those developed by the Atmospheric Radiation Measurement (ARM) program (e.g., Li et al., 2005; Mace and Benson, 2008) and Cloudnet in Eu-

* Corresponding author: Hongbin CHEN
Email: chb@mail.iap.ac.cn

© Institute of Atmospheric Physics/Chinese Academy of Sciences, and Science Press and Springer-Verlag Berlin Heidelberg 2016

rope (e.g., Haeffelin et al., 2005; Illingworth et al., 2007), which are well equipped with ground-based remote sensing instruments, can provide information on the cloud properties over the sites (Zhao et al., 2011, 2012). In addition to ground-based instruments, balloon-mounted radiosondes can penetrate cloud layers and thus provide *in situ* measurements of clouds, which, together with observational temperature, humidity and pressure profiles, can be used to study atmospheric thermodynamic and dynamic processes (Manzato, 2007; Kollias et al., 2009). Radiosonde data with high accuracy and vertical resolution have also been widely deployed to determine the locations and boundaries of cloud layers (e.g., Poore et al., 1995). Wang and Rossow (1995) used relative humidity (RH) profiles to obtain the cloud vertical structure. Chernykh and Eskridge (1996) developed a cloud detection method based on the second-order derivatives of temperature and RH with respect to height. Cloud boundaries are defined if at least one of the two second-order derivatives is zero. Using radiosonde data, many studies have analyzed cloud vertical structure (e.g., Chernykh et al., 2000; Wang et al., 2000; Minnis et al., 2005), but few have been validated due to a lack of trustworthy and/or independent products (e.g., Wang et al., 1999; Naud et al., 2003).

As part of a major U.S.–China joint field experiment, the East Asian Study of Tropospheric Aerosols and their Impact on Regional Climate (Fan et al., 2010; Li et al., 2011), an ARM mobile facility (AMF) was deployed at Shouxian, China in 2008. Using a modified version of the method described by Wang and Rossow (1995), the radiosonde data obtained from the AMF campaign were used to derive the vertical cloud distributions (Zhang et al., 2010). Zhang et al. (2013) further carried out an extensive validation of the cloud retrieval method against a ground-based remote sensing method at multiple ARM sites located in different climate regimes. It was found that the cloud layers derived from the two methods agreed well at the Southern Great Plains (SGP) site located in the midlatitudes; however, the radiosonde tended to detect more cloud layers in the upper troposphere at the tropical western Pacific and north slope of Alaska sites.

As mentioned, many previous studies have focused on the detection of cloud appearance from radiosonde measurements. However, radiosonde data with high vertical resolution also provide a good opportunity to study the dynamics and thermodynamics of clouds, but very few attempts of this type have been made. The dynamic and thermodynamic parameters of clouds can be derived from *in situ* measurements by the radiosonde of temperature, RH and wind vector with high vertical resolution, and its balloon's speed of ascent. More importantly, analysis of the dynamics and thermodynamics of clouds can be performed based on the cloud detection result; therefore, we can explore the potential differences in these parameters within, below and above clouds. This was the aim of the present reported study. This objective was achieved by analysis of the dynamic and thermodynamic characteristics within, below and above low and middle clouds, which were derived from the radiosonde data during the AMF-China campaign. A schematic representation of the analysis procedures is shown in Fig. 1. To achieve this objective, dynamic features, temperature distributions and their inversion structures, convective available potential energy (CAPE), the lifting condensation level (LCL), and equilibrium level (EL) were calculated from the radiosonde measurements. Although CAPE is not a true measure of instability, it is still widely deployed as a predictor of atmospheric instability (Sobel et al., 2004). The LCL is a critical point for convection activities because saturation is required to realize the instability; therefore, it is often used to estimate the cloud-base height (Craven et al., 2002). The EL is generally taken as an important parameter for forecasting the convection cloud-top height in short-term forecasts. The results

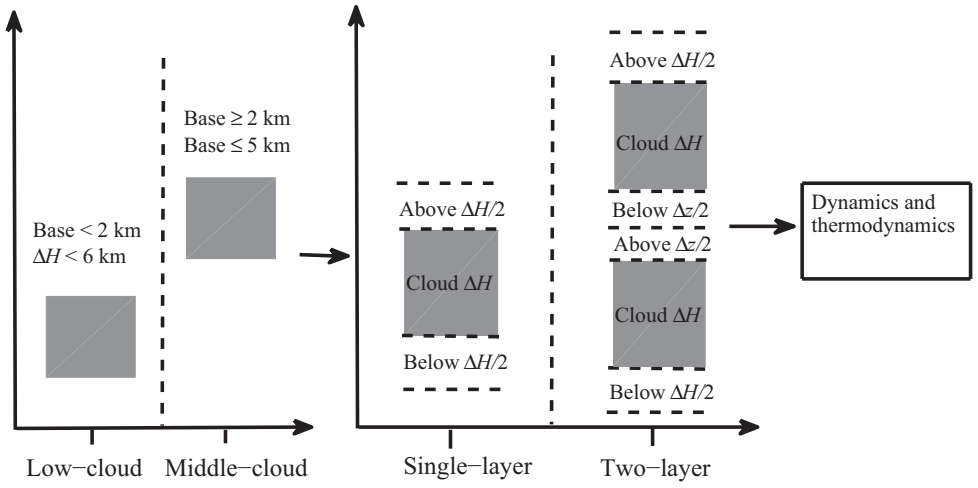

Fig. 1. Schematic representation of the dynamic and thermodynamic study procedures below, within and above clouds. ΔH denotes the thickness of cloud layers shown by the gray rectangular areas, and Δz is the distance between two-layer clouds.

should be beneficial for further understanding of the dynamics and thermodynamics of clouds and their neighboring environment. Potential difference in dynamics and thermodynamics between the cloud layers and clear regions can also help to interpret climate model simulations.

The paper is organized as follows: Section 2 describes the data and algorithms. A detailed investigation of the dynamic and thermodynamic characteristics within, below and above clouds over the AMF-China site is presented in section 3. A discussion and conclusions are provided in section 4.

2. Data and methodology

2.1. *Data description*

The AMF-China site at Shouxian, Anhui Province [(32.56°N, 116.78°E); 21 m above sea level] was in operation from 14 May to 28 December 2008. The observation period can be divided into two parts: (1) the May-to-August Mei-yu season, which is characterized by high humidity and frequent precipitation events associated with the East Asian monsoon system; and (2) the September-to-December dry season. During the campaign period, Vaisala RS92-SGP radiosondes were launched four times a day at 0130, 0730, 1330 and 1930 LST. Profiles of temperature, RH, pressure, wind speed and wind direction at heights from the surface to generally higher than 10 km were measured.

In addition to the radiosonde measurements, ground-based active remote sensing instruments, such as a Vaisala ceilometer and a Micropulse Lidar (MPL) were also employed to detect clouds during the entire campaign period of AMF-China. Furthermore, a 95 GHz W-band ARM cloud radar (WACR) that can detect multiple cloud layers was installed from 15 October to 15 December 2008. By combining observations from the cloud radar, the MPL and the ceilometer, the Active Remote Sensing of Cloud (ARSCL) value-added product (VAP) was generated by the ARM scientists to provide cloud boundaries with the best possible accuracy (Clothiaux et al., 2000; Kollias et al., 2009). The ARSCL VAP has a temporal resolution of five seconds and a vertical resolution of 45 m. Up to 10 cloud-layer boundaries can be identified in the ARSCL VAP product. Table 1 illustrates the various datasets and their applications in locating the cloud layers. In this study, we mainly used the radiosonde data to derive the cloud layers and then investigated the dynamics and thermodynamics associated with the cloud layers. The ARSCL data were employed to aid the radiosonde measurements to locate the cloud layers if they were available.

2.2. *Method*

2.2.1. *Cloud detection and classification using radiosonde data*

We used the radiosonde-based cloud retrieval algorithm of Zhang et al. (2013), which was modified from Wang and Rossow (1995), to detect cloud boundaries. The algorithm employed three height-resolving RH thresholds to determine cloud layers, i.e., the minimum and maximum RH thresholds in cloud layers, as well as the minimum RH threshold within the distance of two neighboring cloud layers. A detailed description of the algorithm can be found in Zhang et al. (2013).

Low clouds were defined by their bases being lower than 2 km and their thicknesses less than 6 km. Clouds with their bases ranging from 2 to 5 km were defined to be middle clouds. Only single- and two-layered low and middle clouds are discussed in this paper. The cloud-free layers above and below clouds were defined as follows: For the single-layer cloud, the cloud-free layer above the cloud layer was determined as the layer ranging from the cloud top upwards to half of the cloud thickness (ΔH) level (Fig. 1). Below the cloud layer it was defined in a similar way but ranging from the cloud base downwards to the $\Delta H/2$ level. If the distance between the cloud base level to the surface was less than $\Delta H/2$, it was determined to be from the cloud base downwards to the surface. For cases with two-layer clouds, the cloud-free layer below the higher cloud layer was set to be the upper half of the cloud-free layers between the two-layer clouds (Δz). The cloud-free layer above the lower cloud layer was determined to be the lower half of the cloud-free layer between the two-layer clouds. The determination of the cloud-free layer above the higher cloud layer and below the lower cloud layer was the same as that for the single-layer cloud.

2.2.2. *Dynamic and thermodynamic characteristics*

Dynamic features of the atmosphere were derived from the horizontal wind speed and the balloon speed of ascent. The temperature structures, including the temperature inversion layers associated with the cloud layers were also investigated. In addition, three convective parameters (CAPE, LCL and EL) are discussed in this paper.

CAPE is a vertically integrated index and measures the cumulative buoyant energy in the free convective layer (FCL) ranging from the level of free convection (LFC) to the EL. The LFC is the level at which the parcel temperature exceeds the ambient temperature and parcels are unstable relative to their environment. The EL is the level at which the ambient temperature exceeds the parcel temperature and parcels are stable relative to their environment. The formal definition of

Table 1. Information on the datasets used in this study and their applications.

Dataset	Date range	Temporal resolution	Applications
Radiosonde	14 May to 28 December 2008	4 times per day	Cloud layer retrievals; dynamics and thermodynamics associated with cloud layers
ARSCL	15 October to 15 December 2008	5 s	Cloud structure retrievals; as complementary data to the radiosonde data for cases studies of temperature structures

CAPE, adopted from Doswell III and Rasmussen (1994), is expressed as

$$\mathrm{CAPE} = g\int_{Z_{\mathrm{LFC}}}^{Z_{\mathrm{EL}}}\left(\frac{T_{\mathrm{vp}}-T_{\mathrm{ve}}}{\overline{T_{\mathrm{ve}}}}\right)dz, \qquad (1)$$

where T_{vp} is the virtual temperature of the parcel (units: K); T_{ve} is the virtual temperature of the environment (units: K); Z_{EL} is the EL height (units: m), which is generally obtained from a T-ln$p$ diagram; Z_{LFC} is the LFC height (units: m); $\overline{T_{\mathrm{ve}}}$ (units: K) is the mean potential temperature in the FCL; and g is the gravitational acceleration (units: N kg^{-1}).

The widely used Espy's equation (Espy, 1841), for the relationship between the LCL and dew-point temperature, is deployed to compute the LCL and is given by

$$\mathrm{Z_{LCL}} = 125(T - T_{\mathrm{d}})\ , \qquad (2)$$

where Z_{LCL} is the LCL height (units: m), T is the temperature (units: °C), and T_{d} is the dew-point temperature (units: °C).

There are likely several temperature inversion layers that are separated above the cloud top. To ensure that the temperature inversion is related to the cloud as far as possible, only the first temperature inversion layer above the cloud top is discussed in this paper. The method used to obtain the temperature inversion layer is the first-order derivative of the temperature profile with respect to height. The contiguous levels with the first-order derivative larger than zero are treated as the temperature inversion layer. Taking into account the complex structures of radiosonde-based temperature profiles, there may be very thin layers not determined as temperature inversion layers located between two temperature inversion layers separated by a very short distance. To obtain reliable results, two neighboring temperature inversion layers are considered as one layer if the distance between these two layers is less than 50 m. The Vaisala RS92 radiosonde measures data every 2 s, with an average speed of ascent of about 5 m s^{-1}, resulting in a vertical resolution of about 10 m (5 m s^{-1} × 2 s). The thickness of the temperature inversion layer needs to be larger than 15 m by considering that the temperature inversion layer should be larger than the vertical resolution of the radiosonde. In order to derive the temperature inversion layer that is close to the cloud top and thereby related to the cloud processes, the distance between the base of the temperature inversion layer and the cloud-top height should be properly considered. The occurrence frequency of the temperature inversion above the single-layer top height was 66%, 68%, 71% and 71% if the distance was set to be 50 m, 100 m, 200 m and 300 m, respectively. Although the occurrence frequency varied little, the thickness of the temperature inversion layer changed to some extent. Based on visual inspection, we found that reliable results were obtained by setting the distance as 200 m, and so this distance was used in the study.

3. Results

3.1. *Cloud vertical distributions over the Shouxian site*

Figure 2a shows the cloud-top height frequencies (CTFs) for all cloud samples derived from the radiosonde during the whole campaign period, in the wet season and the dry season, as well as the CTFs derived from ARSCL data in the dry season. There were three peaks of CTFs for the radiosonde retrievals during the whole period, which were located at 1, 9.5 and 12.5 km, respectively. The cloud-top heights in the wet season were generally higher than those in the dry season. The pattern of CTFs was similar between the ARSCL data and the radiosonde data collected during the dry sea-

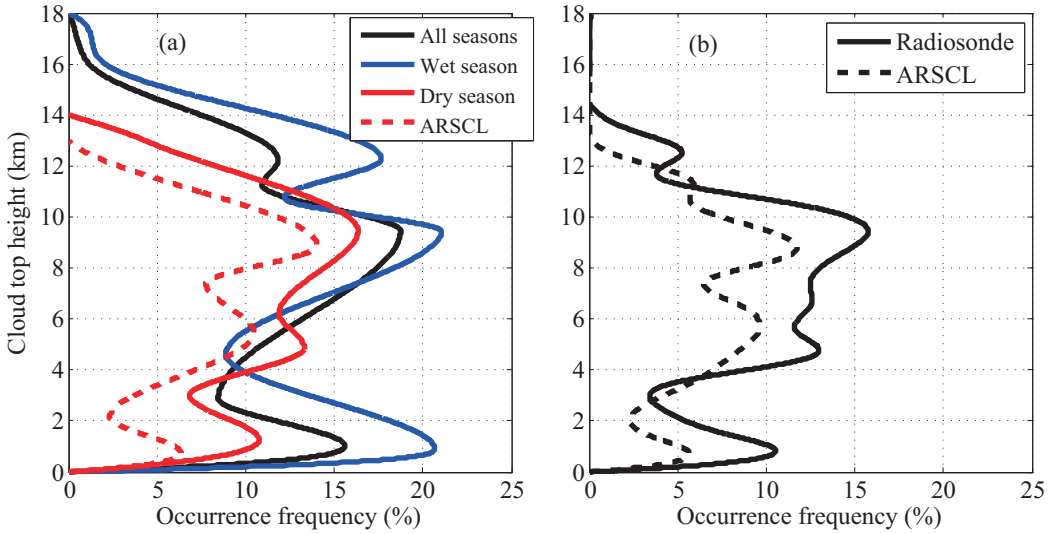

Fig. 2. (a) Frequency distributions of cloud-top heights derived from the radiosonde observations during the entire AMF-China period (black solid line), in wet season (blue solid line), in dry season (red solid line); and frequency distributions obtained from the ARSCL data (red dashed line). (b) As in (a) but for cloud-top heights obtained from the subset of the radiosonde and ARSCL dataset generated at their simultaneously observed time.

son. However, the magnitude of cloud frequencies detected by ARSCL was significantly lower than those detected by radiosonde, which was likely due to the following three factors: (1) the difference of the objects detected by two instruments caused by the balloon's drift and fixed ground-based observation (Zhang et al., 2013); (2) the incomplete overlapping observational period associated with the diurnal cycle of the cloud occurrence (e.g., Zhang and Klein, 2010); and (3) the different observation temporal intervals between the two cloud products (Zhang et al., 2014). Figure 2b presents the CTF distributions obtained from the radiosonde and ARSCL at concurrent observation time, in which a large decrease of the differences in the CTFs between the two cloud products is revealed, as compared with Fig. 2a. It has been proven that the calculated cloud occurrence frequency will increase as the sample temporal intervals increase (Xi et al., 2010). The sample temporal interval of ARSCL data used in this study was 5 s. However, a radiosonde generally spends ∼90 min in the atmosphere to collect data during one launch, which will result in higher cloud occurrence frequency calculated than the ARSCL measurements. Differences in the CTFs at the low and high atmospheric column levels were larger than those in the middle troposphere. The radiosonde cloud retrievals tended to be larger than the ARSCL detections at the layer above 4 km, with a maximum difference of ∼7%. Besides the three reasons mentioned above, the deficiency of high-level clouds in the ARSCL cloud products was also likely caused by the attenuation effect of thick lower-level clouds and/or fog in the cloud detection of the ground-based remote sensing instruments (Protat et al., 2014).

The number (percentage) of occurrences for the radiosonde detecting at least one cloud layer and non-cloud layer was 652 (80.2%) and 161 (19.8%), respectively. By using 10 years of data collected over the ARM SGP site, we found that the radiosonde-based cloud occurrence frequency was 65% (Zhang et al., 2014). The radiosonde-based cloud occurrence at the AMF-China site was about 15% larger than that at Taihu Lake (65%), which was about 500 km away from AMF-China (Zhao et al., 2014). The frequency of radiosonde measurements determining single- and two-layered low- and middle-cloud is presented in Table 2. The number (frequency) for the radiosonde detecting one-layer cloud was 92 (11.3%), of which 51 and 41 were single-low and single-middle clouds, respectively. There were 39 (4.8%) two-layer clouds, of which 4 and 8 were two-layer-low and two-layer-middle clouds, respectively. The total number of low/middle cloud layers analyzed in this study was 86/84. To present the potential differences of the dynamic and thermodynamic properties between the low and middle clouds, a few comparisons were conducted at times between single-layered low and middle clouds, excluding the two-layered low and middle clouds due to their small numbers mentioned above (4 and 8).

The probability density function (PDF) of cloud-base height and cloud-top height of single-layer clouds and the layers below and above the two-layer clouds is shown in Fig. 3. The greatest PDF (∼0.3) occurred for cloud-base heights of <0.5 km and cloud-top heights of >5 km for the single-layer clouds (Fig. 3a). With regard to the layer below two-layer clouds, their base/top heights were lower than 0.5/2 km for 41%/35% of the cases analyzed (Fig. 3b). The largest PDF of both cloud-base height and cloud-top height was located at ∼5 km for the layer above two-layer clouds (Fig. 3c). The radiosonde launches were further divided into four groups based on measurements from four radiosonde launches per day to recognize the cloud distributions at 0130, 0730, 1330 and 1930 LST. The percentages of single-layer cloud occurrences were 26.1%, 32.6%, 19.6% and 21.7% at the four launch times, respectively (Table 2). The two-layer clouds occurred most frequently in the morning (0730 LST) and at noon (1330 LST). In general, clouds occurred most often at noontime or in the early afternoon (1330 LST). This finding was consistent with previous results obtained over West Africa (e.g., Rickenbach et al., 2009; Bouniol et al., 2012), which might be associated with locally generated convection during this time.

Table 2. The occurrence number (frequency) of radiosonde-retrieved single- and two-layered low and middle clouds, and their percentage occurrences at four launch times (LST).

	Number	Percentage			
	(Frequency)	0730	1330	1930	0130
Single-layer clouds	92 (11.3%)	26.1	32.6	19.6	21.7
Two-layer clouds	39 (4.8%)	30.8	30.8	18.0	20.5

3.2. *Dynamic features*

The frequency distributions of horizontal wind direction and speed within, below and above clouds are shown in Fig. 4. For the single-layer cloud, the wind direction was generally spread over all directions below the cloud; however, the prevailing wind direction was west within and above the cloud. The occurrence frequencies of air advection with wind speed less than 10 m s^{-1} were 70%, 34% and 17% below, within and above the cloud, respectively. The horizontal wind speed was seldom greater than 30 m s^{-1} below cloud; however, their percentages were 21% and 47% within and above cloud. In general, the horizontal wind speed was higher above the cloud layers than within and below the cloud. With regard to single-low clouds, their wind distributed throughout all directions, with most speeds less than 10 m s^{-1} (84%); the major wind direction was west, with about half of wind speeds larger than 20 m s^{-1} (52%) within the single-middle clouds (figure not shown). For two-layer clouds, the horizontal wind speeds were generally less than 20 m s^{-1} below, within and above cloud for the low-layer cloud. Higher wind speed was observed in the upper-layer clouds than in the lower-layer clouds. The wind dispersed in many directions in the lower layer, but the prevailing wind direction was west for the upper layer. Meanwhile, the pattern was similar for wind direction distributions within and above cloud obtained from the upper-layer clouds and the single-layer clouds.

Figure 5 shows the frequency distributions of the balloon's speed of ascent below, within and above the cloud. For

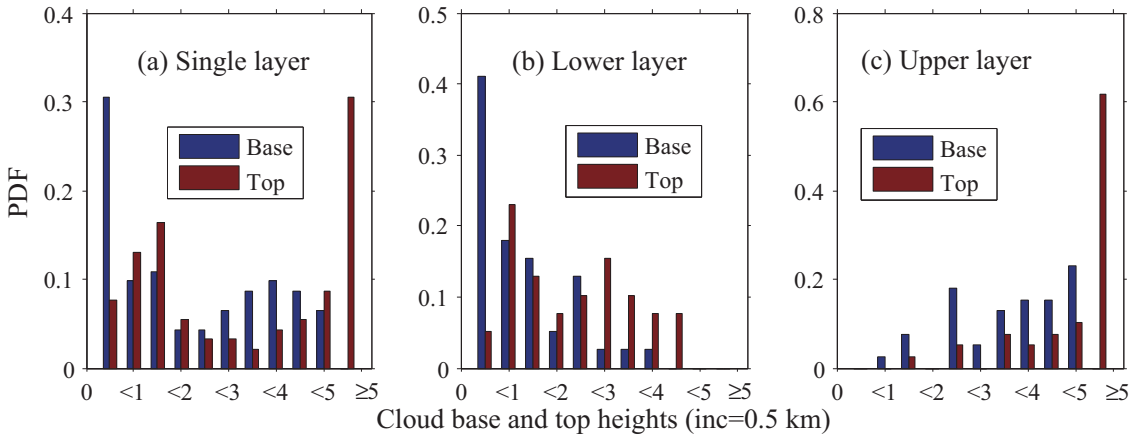

Fig. 3. Probability density function (PDF) of cloud-base height (blue bars) and cloud-top height (red bars) for (a) single layer cloud, and (b) the lower layer and (c) upper layer of two-layer clouds. The step width is 0.5 km.

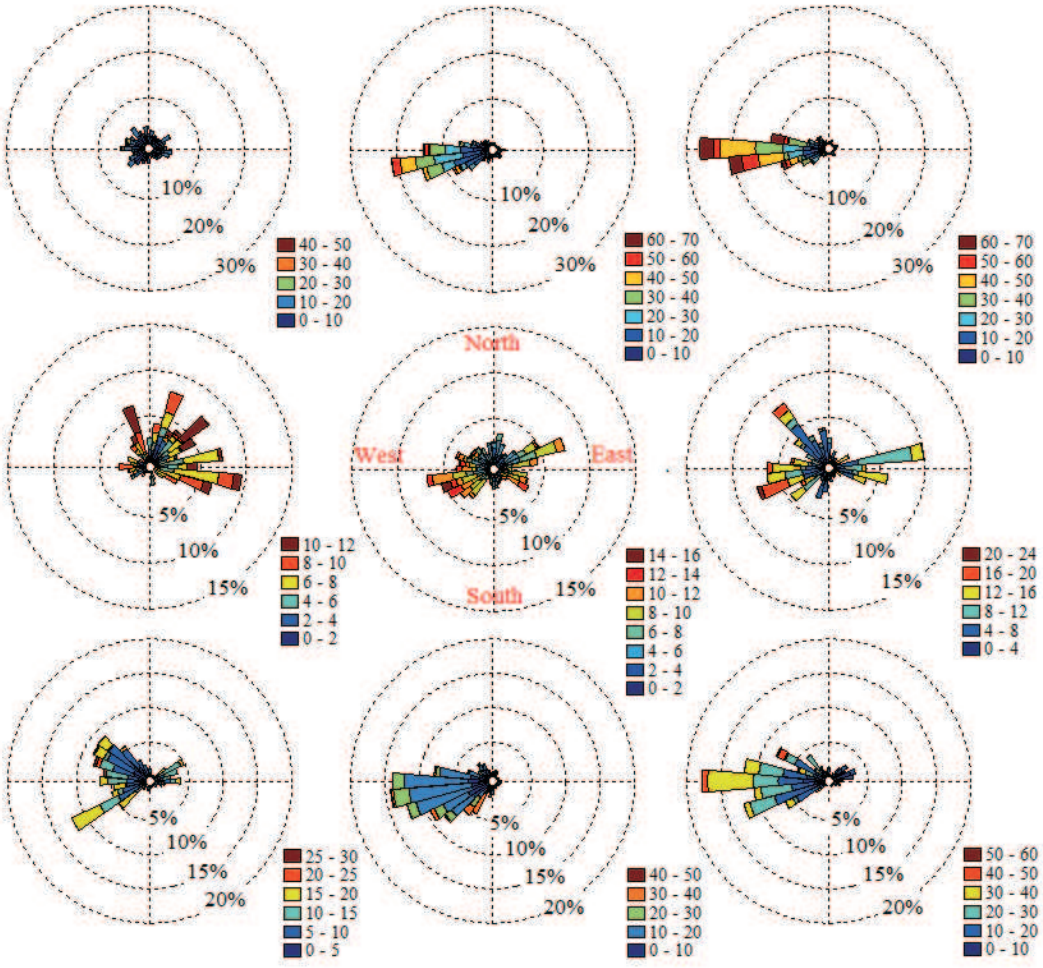

Fig. 4. The occurrence frequency of horizontal wind direction and speed below (left panels), within (middle panels) and above (right panels) clouds. Top, middle and bottom plots denote single-layer cloud, and the lower and upper cloud of two-layer clouds, respectively.

the single-layer cloud (Fig. 5a), there were large frequency distributions between 4 and 6 m s^{-1} for the balloon's speed of ascent within (72%) and below (84%) cloud. The frequency was 65% for the balloon's speed of ascent ranging from 3 to 5 m s^{-1} above the cloud. The maximum frequencies of ascent speed were 5.6, 5.2 and 4.1 m s^{-1} within, below and

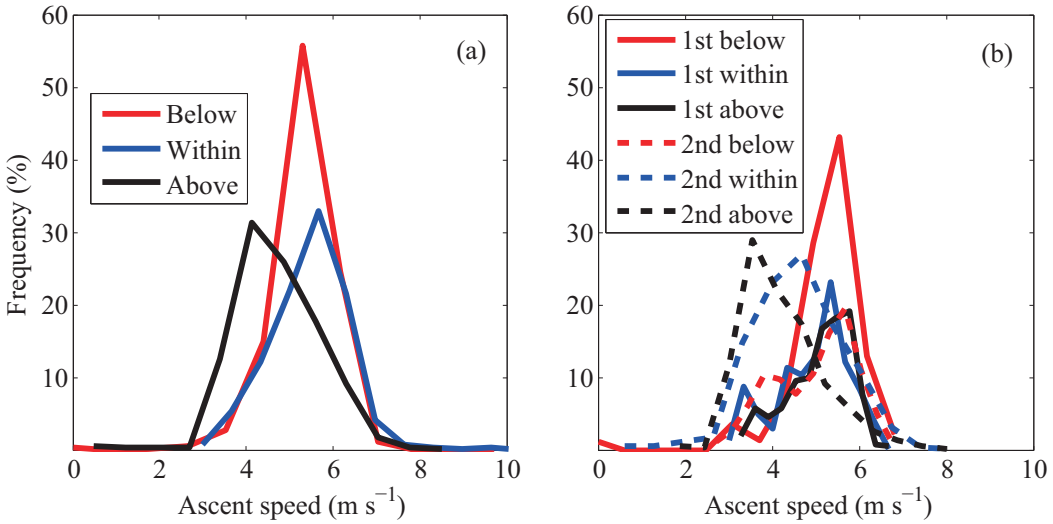

Fig. 5. Frequency distributions of balloon ascent speed within (blue line), below (red line) and above (black line) cloud for (a) single-layer cloud and (b) two-layer clouds. The solid lines and dashed lines in (b) represent lower and upper cloud, respectively.

above the cloud. In general, the largest balloon ascent speed was observed within the cloud layers, followed by below the cloud, and finally above the cloud, which suggested the strongest upward flow occurred in the cloud. The balloon's ascent speeds were less than 6 m s^{-1} for 80%/77% within single-low/middle clouds (figure not shown). The occurrence frequencies of large ascent speed episodes (>8 m s^{-1}) were 1% within single-low clouds—two times larger than within single-middle clouds. For two-layer clouds (Fig. 5b), the balloon ascent speeds derived from the lower-level cloud were generally larger than those from the upper-layer clouds, partly implying that the uplifted movement was stronger in the lower atmosphere than at higher levels. It should also be noted that the smaller balloon ascent speed above the upper-layer cloud was due in part to an increase of balloon–radiosonde weight caused by liquid water wetting.

The profiles of average balloon ascent speed and radiosonde-based vertical cloud occurrence frequency at a vertical resolution of 200 m from the surface to 4 km are shown in Fig. 6. The vertical cloud occurrence frequency was defined as the number of radiosonde samples detecting a cloud or portion of cloud anywhere within a specified 200 m bin divided by the total number of radiosonde samples during the AMF campaign period. It can be seen that the cloud occurrence frequency ranged between 17% and 25%. The cloud occurrence frequency increased from 0.2 to 0.7 km and reached a maximum (24.4%) at 0.7 km. Similarly, Zhao et al. (2014) also found maximum cloud occurrence over Taihu Lake at a height close to 1 km. The balloon's speed of ascent decreased from the surface upwards to 0.3 km, and then an obvious increase occurred before reaching a maximum (5.3 m s^{-1}) at 0.6 km. The maximum balloon ascent speed was located in the vicinity of the maximum cloud occurrence frequency. This was likely due to the occurrence of distinct upward motions typically ranging from 0.10 to 0.16 m s^{-1}

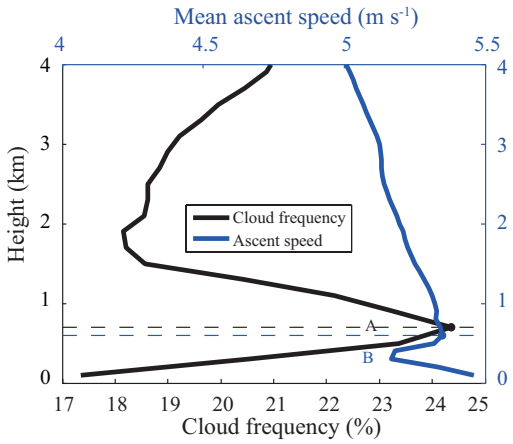

Fig. 6. The relationship between cloud vertical distribution frequency (black line) and the balloon's mean speed of ascent (blue line) as a function of detection altitude. Points A and B display the locations of the maximum cloud frequency and maximum ascent speed.

within the clouds, which was consistent with the results presented by Cotton and Anthes (1989).

3.3. *Thermodynamic features*

The frequency distributions of radiosonde-based temperature gradient within, below and above the cloud are shown in Fig. 7. The temperature gradient every 1000 m was defined as $(T_{i+1} - T_i) \div (D_{i+1} - D_i) \times 1000$, where D_i is the detecting altitude of a certain level and T_i is the temperature of this level. Results for single- and two-layer clouds are shown in Figs. 7a and b, respectively. The largest frequency was observed for the temperature gradient less than 5°C km^{-1} for single- and two-layer clouds. For single-layer cloud, the temperature inversion structures (>0°C km^{-1}) occurred most of-

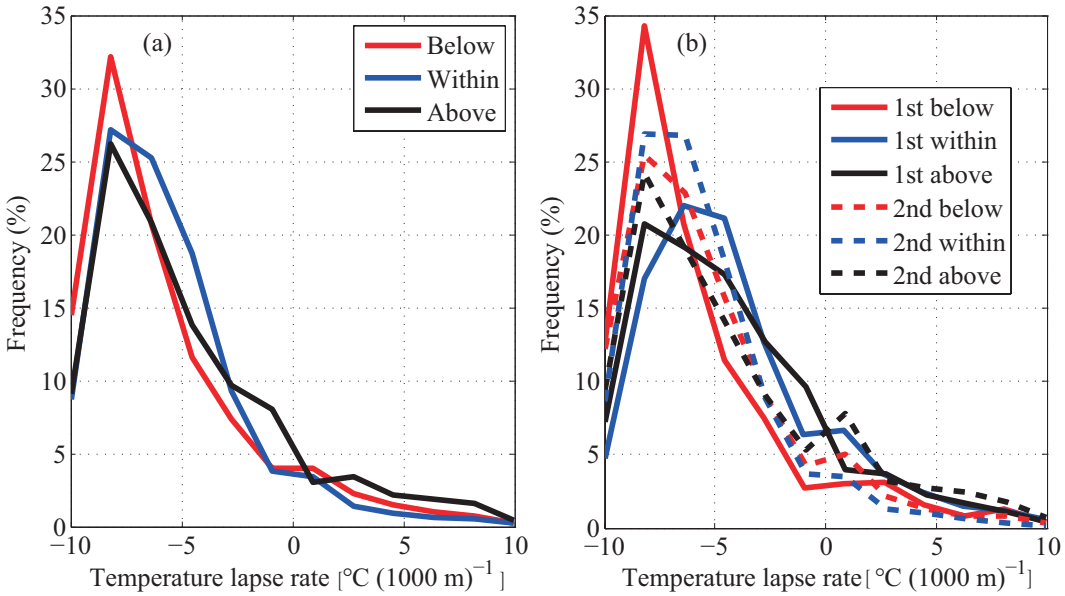

Fig. 7. As in Fig. 5 but for the temperature gradient.

ten above the cloud layer, followed by below the cloud, and a minimum within the cloud. For two-layer cloud configurations, the frequency distributions were similar between the two layers. The temperature inversion structures below and within the cloud layer occurred less frequently for the upper layer than the lower layer. However, the temperature inversion occurrence frequency above the cloud was larger for upper cloud (16%) than for lower cloud (14%), which demonstrated that there were stronger temperature inversion structures for upper clouds.

Figure 8 displays two radiosonde-retrieved cloud cases and the temperature inversion structures above the cloud top. Gray areas in Figs. 8a and c represent radiosonde-derived cloud layers, and rectangles outlined with red dashes denote temperature inversion locations. Figure 8a presents the single-layer cloud for the radiosonde launched at 0128 LST 15 November 2008 and Fig. 8c shows the two-layer clouds obtained from the radiosonde launched at 0724 LST 8 November 2008. Figures 8b and d show the cloud mask derived from the ARSCL around the radiosonde launch time in Figs. 8a and c. Although there was larger temporal variation for cloud locations and cloud thickness in the ARSCL data, the cloud layer structures obtained from the two distinctly different approaches agreed well. An obvious temperature inversion layer was determined above the single-layer cloud (Fig. 8a). The temperature inversion layer thickness (T_t), temperature inversion magnitude (T_m) (defined as the temperature difference collected at the top height and base height of the temperature inversion layer), and the temperature inversion gradient every 100 m (defined as $T_m/T_t \times 100$) were 415.1 m, 3.1°C and 0.7°C (100 m)$^{-1}$, respectively. There was no noticeable temperature inversion layer for the lower-level cloud in two-layer clouds (Fig. 8c). One thin temperature inversion layer was detected above the upper cloud top. The thickness, temperature inversion magnitude and temperature inversion gradient were 90.1 m, 3.3°C and 3.6°C (100 m)$^{-1}$, respectively. It was evident that the temperature inversion structures were well derived by using the algorithm specified in section 2.

In terms of the radiosonde-based temperature inversion retrievals located above the single-layer cloud-top height, most of their thicknesses were less than 200 m, with a percentage of 85% and maximum thickness of ~415 m. The inversion magnitude was generally less than 2°C and the maximum magnitude was 6.6°C. The occurrence frequencies were 57% and 20% for gradients less than 1°C (100 m)$^{-1}$ and ranging from 1 to 2°C (100 m)$^{-1}$, respectively. The average temperature inversion layer thickness, magnitude and gradient for all single-layer (low and middle) clouds were 117 ± 94 m, 1.3 ± 1.3°C and 1.4 ± 1.5°C (100 m)$^{-1}$, respectively (Table 3). The occurrence frequency of the temperature inversion was 71% above all single-layer clouds, which was 80% (59%) above the single-low (middle) clouds. The average temperature inversion magnitude was the same (1.3°C) for single-low and single-middle clouds; however, a larger gradient [1.7 ± 1.8°C (100 m)$^{-1}$] and smaller thickness (94 ± 67 m) were detected above single-low clouds relative to those above single-middle clouds (Table 3). In terms of two-layer clouds, the temperature inversion layer occurrence number (frequency) above the upper cloud-top height was 21 (54%), which was larger than 14 (36%) obtained above the lower cloud-top height. Meanwhile, the temperature inversion layer thickness, magnitude and gradient were also larger when presented by the upper layer [106 ± 59 m, 1.0 ± 0.9°C and 1.0 ± 1.0°C (100 m)$^{-1}$] than by the lower clouds [82 ± 60 m, 0.6 ± 0.9°C and 0.7 ± 0.6°C (100 m)$^{-1}$]. In general, the temperature inversion structures above the cloud-top heights were stronger when presented by one layer than two; and as for two-layer clouds, they were more strongly derived from the upper layer than the lower layer. This may be explained

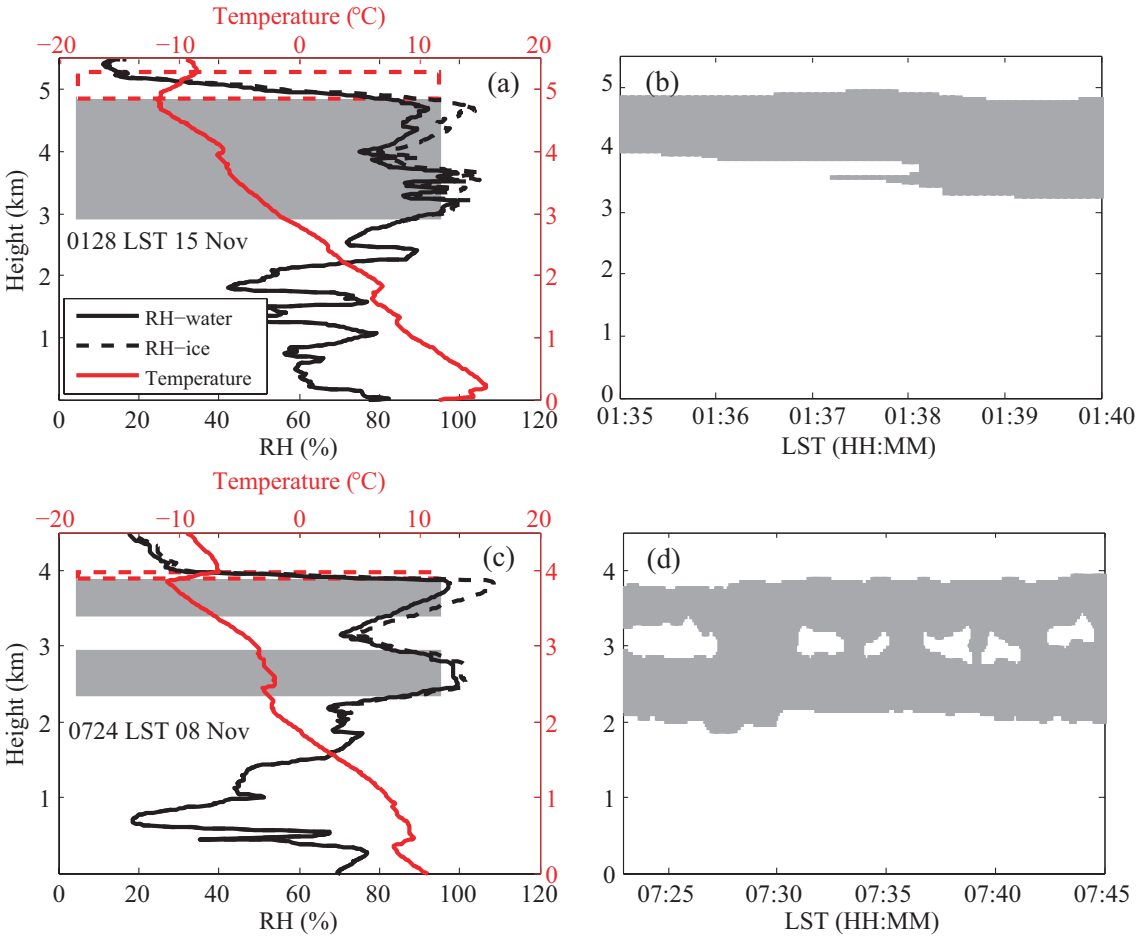

Fig. 8. Radiosonde-retrieved temperature inversion structures above the cloud-top heights for cases of (a) single- and (c) two-layer clouds. Radiosonde vertical profiles of RH with respect to water, RH with respect to ice when temperatures were less than 0°C, and temperature are shown by the solid black line, the dashed black line, and the red line, respectively. Gray areas represent radiosonde-derived cloud layer boundaries, and rectangles outlined by red dashes denote temperature inversion locations. Panels (b) and (d) show the cloud mask obtained from the ARSCL around the radiosonde launch time corresponding to panels (a) and (c), respectively.

Table 3. The occurrence frequency, average temperature inversion layer thickness, magnitude and gradient for all single-layer clouds (All), single-low clouds only (Low), single-middle clouds only (Middle), lower-layer (Lower) and upper-layer (Upper) of two-layer clouds.

		Occurrence frequency	Thickness (m)	Magnitude (°C)	Gradient [°C (100 m)$^{-1}$]
Single-layer clouds	All	71%	117 ± 94	1.3 ± 1.3	1.4 ± 1.5
	Low	80%	94 ± 67	1.3 ± 1.5	1.7 ± 1.8
	Middle	59%	157 ± 120	1.3 ± 1.0	0.9 ± 0.7
Two-layer clouds	Lower	36%	82 ± 60	0.6 ± 0.9	0.7 ± 0.6
	Upper	54%	106 ± 59	1.0 ± 0.9	1.0 ± 1.0

by the radiative energy exchanges that affect the thermodynamic state of cloud layers, as well as the interactions between the two layers of cloud. The emission of infrared radiation at the top of a cloud will act to produce marked cooling around the top of the cloud layer (Chernykh and Eskridge, 1996), which results in the temperature inversion structures above the cloud-top heights of single-layer and the upper layer of two-layered clouds. However, this longwave radiative cooling effect is strongly reduced at the top of the lower layer of cloud in the presence of upper layers of cloud (Chen and Cotton, 1987; Wang et al., 1999). The diurnal variation of temperature inversion structures above the cloud top at the AMF-China site (shown in Fig. 9) was investigated based on measurements collected from four radiosonde launches per day. Temperature inversion structures occurred most frequently at 1330 LST (32%) and least at 1930 LST (18%) for single-layer cloud. The patterns were similar for frequency distributions obtained from the upper-level

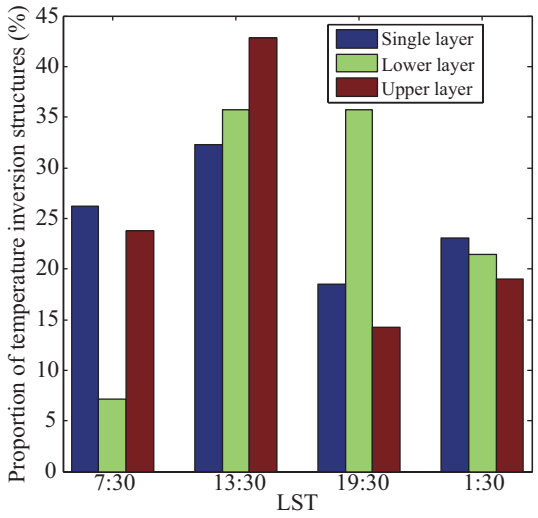

Fig. 9. The proportion of temperature inversion structures located above the cloud-top heights occurring at four radiosonde launch times. The single-layer cloud, and the lower layer and upper layer of two-layer clouds are shown by the blue bars, green bars and red bars, respectively.

cloud of two-layer clouds and the single-layer cloud, but the percentage was larger for the former (43%) than the latter (32%) at noontime (1330 LST). More temperature inversion structures occurred at noontime and in the evening (1930 LST) for the lower-level cloud of two-layer clouds, and least in the morning (8%). Overall, the temperature inversion structures above the cloud top tended to occur most frequently at noontime for both single- and two-layer clouds.

The mean temperature profiles under cloudy and cloud-free conditions at noontime (1330 LST) and nighttime (0130 LST) were also examined (figure not shown). About 50% of the cloudy skies occurred during the warm months (June, July and August); meanwhile, most of the clear skies ($\sim$51%) occurred during the cold months (November and December). Because of the heterogeneous distributions of sky conditions, the mean temperature was higher in cloudy skies than in clear skies from the surface to about 12 km with a maximum difference at 10.5 km.

Figure 10 shows the mean monthly variations of temperature at cloud-base height, cloud-top height, and cloud center level and their distance from the 0°C height level for the single- and two-cloud layers. The temperature was generally higher than 0°C before October for single-layer cloud, and a similar pattern was revealed at cloud-base height, top-height, and cloud center level (Fig. 10a). The structure of distance from the 0°C height level (Fig. 10b) mirrored that of temperature. For the lower layer of two-cloud layers (Figs. 10c and d), the temperature (the distance from the 0°C height level) generally reached maximum (minimum) in August (November) for cloud-base height, top-height and cloud center level. The temperature of the upper layer (Fig. 10e) was lower than 0°C at the cloud center and top levels during most seasons, which was higher than 0°C for the cloud base from May to October (Figs. 10e and f).

3.4. *CAPE, LCL and EL*

The CAPEs derived from the AMF radiosonde data collected in Shouxian were mostly greater in the wet season than the dry season. It was found that 99.5% of the CAPEs were smaller than 500 J kg^{-1} in the dry season and 62% in wet months. The radiosonde-based lowest cloud boundaries were compared with the LCL and EL calculated from the radiosonde measurements during the entire AMF-China period. The cloud-base heights were generally located higher than the LCL, accounting for 68.5%. This should be mainly because the adiabatic assumption of air mass in calculating the LCL was not strictly satisfied during the vertical motion of stratiform layers. The correlation coefficient between the detected cloud-base heights and calculated LCL was 0.39. The relationship between the cloud-top heights and EL was also not high. Absolute differences between the cloud-base heights and LCL were less than 0.5 km for 51.6% of the cases analyzed, which were less than 0.5 km for 33.8% between the cloud-top heights and the EL. In general, no clear relationship was found between the cloud-base height (cloud-top height) and LCL (EL). This was likely because there were very few cases of intense convection, which did not allow us to derive a clear relationship between the observational data and calculated convective parameters. The above comparisons were further conducted for the radiosonde samples collected in summer months (June, July and August) when convective clouds often occurred. Relative to the entire AMF-China period, their agreement was much better in summer with the absolute differences less than 500 m between cloud-base height (cloud-top height) and LCL (EL) for 66.4% (36.8%) of the cases analyzed. The AMF campaigns at Shouxian lasted less than one year, so the above results associated with the convective parameters were acquired from a relatively short-term period and thereby their representativeness needs to be thoroughly discussed in the future. Further study using long-term data collected at the ARM fixed stations is required.

4. Discussion and conclusions

The U.S. Department of Energy (DOE) ARM-AMF was deployed at Shouxian, Anhui Province, China for more than seven months from 14 May to 28 December 2008. During the AMF campaign, Vaisala RS92 radiosondes were launched four times a day. The cloud vertical structures were derived from the radiosonde measurements (Zhang et al., 2013). The present study focused on the dynamic and thermodynamic characteristics, including horizontal wind speed, the balloon's speed of ascent and the temperature structures, for single- and two-layered low and middle clouds. These dynamic and thermodynamic parameters within-, below- and above-cloud were compared. Meanwhile, a few comparisons were also conducted between the single-low and single-middle clouds to discuss the potential dynamic and thermodynamic differences in low and middle clouds. Highlights of

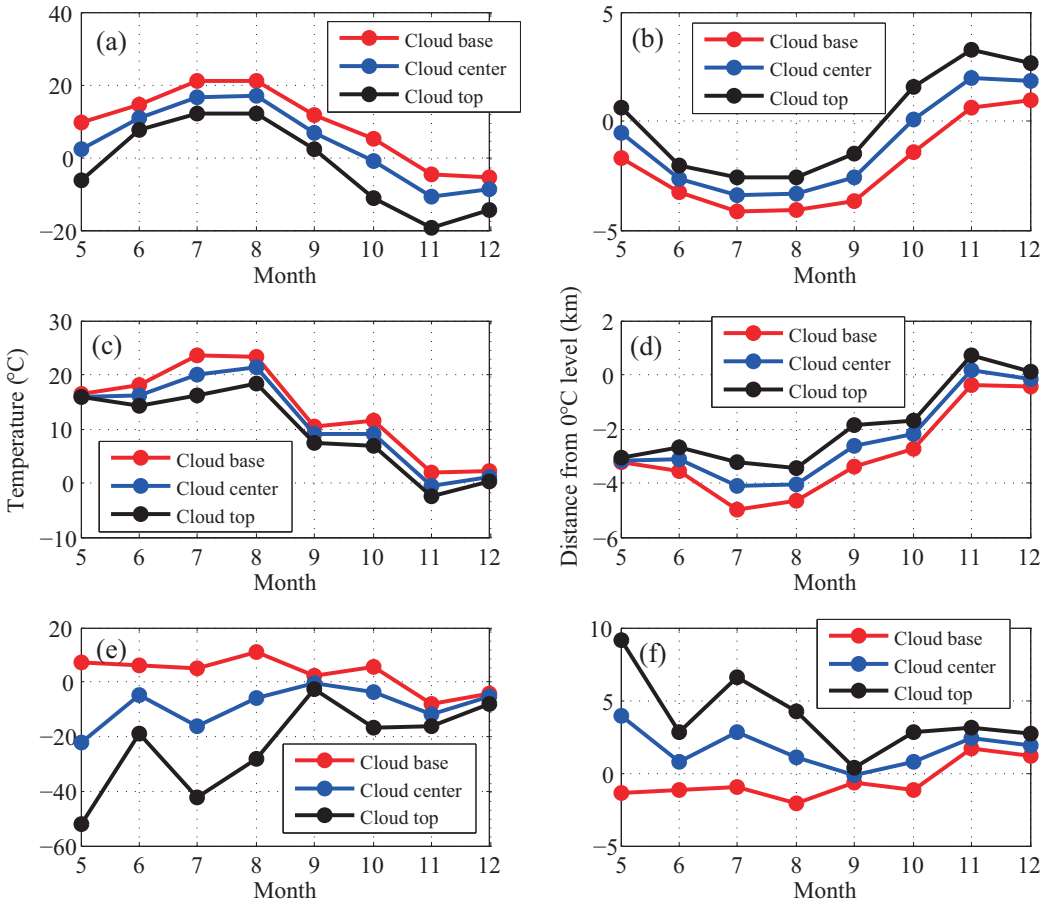

Fig. 10. The monthly mean variations of (a, c, e) temperature at cloud-base height (red line), cloud center level (blue line) and cloud-top height (black line), and their (b, d, f) distance from the 0°C height level for (a, b) single-layer cloud, and (c, d) the lower layer and (e, f) upper layer of two-layer clouds.

the study's findings are summarized as follows:

(1) The horizontal wind speeds were larger above the cloud layers than those observed within and below the cloud for single-layer cloud. The frequency was 84% (52%) for wind speeds of <10 (>20) m s^{-1} in single-low (middle) clouds. For two-layer clouds, the horizontal wind speeds of the upper-layer cloud were generally higher than those of lower-layer retrievals. The prevailing wind direction was west within and above the cloud obtained from upper- and single-layer clouds.

(2) The largest balloon ascent speed was derived within the cloud layers, followed by the rate below the cloud and above the cloud. More large ascent speed episodes ($>$ 8 m s^{-1}) were observed in single-low clouds than in single-middle clouds. The maximum balloon ascent speed was 5.3 m s^{-1}, located in the vicinity of the layer with maximum cloud occurrence frequency (24.4%), suggesting upward motions (typically of 0.10–0.16 m s^{-1}) occurred within cloud layers.

(3) The average temperature inversion layer thickness, magnitude and gradient above all single-layer (low and middle) clouds were 117 ± 94 m, 1.3 ± 1.3°C and 1.4 ± 1.5°C (100 m)$^{-1}$, respectively. The average temperature inversion magnitude was the same (1.3°C) for single-low and single-middle clouds; however, a larger gradient [1.7 ± 1.8°C (100 m)$^{-1}$] and smaller thickness (94 ± 67 m) were detected above single-low clouds relative to those above single-middle clouds [0.9 ± 0.7°C (100 m)$^{-1}$ and 157 ± 120 m]. For two-layer clouds, the temperature inversion parameters of the upper layer were 106 ± 59 m, 1.0 ± 0.9°C and 1.0 ± 1.0°C (100 m)$^{-1}$, respectively, which were larger than those of the lower-clouds [82 ± 60 m, 0.6 ± 0.9°C and 0.7 ± 0.6°C (100 m)$^{-1}$]. In general, the temperature inversion structures above the cloud-top heights of one-layer clouds were stronger than those of two-layer clouds; for two-layer clouds, stronger temperature inversions were observed for the upper layer clouds as compared with the lower layer clouds. This feature should be associated with the radiative energy exchanges that affected the thermodynamic state of cloud layers, as well as the interactions between the two layers of cloud. Temperature inversions occurred most frequently at noontime.

(4) The CAPE was greater during the wet season than the dry season. Absolute differences between the cloud-base height (cloud-top height) and LCL (EL) were less than 0.5

km for 66.4% (36.8%) of the cases analyzed in summer.

The dynamic and thermodynamic characteristics associated with the low and middle clouds were discussed in this study. However, the 2008 AMF campaigns at Shouxian lasted less than one year, so the results presented in this study were acquired from a relatively short-term period and thereby their representativeness needs to be thoroughly discussed in the future. In addition to the mobile facility, intensive and long-term (more than 10 years) measurements of surface and atmospheric quantities have been carried out at the fixed ARM sites, such as the U.S. SGP, northern slope of Alaska, and tropical western Pacific sites. Furthermore, as shown in previous studies (e.g., Protat et al., 2014; Zhang et al., 2014), the cloud retrievals from radiosonde, space-borne and ground-based remote sensing instruments have different merits and limitations. As the next step, the long-term data (radiosonde and ground-based measurements) collected from these fixed stations will be used together with space-borne remote sensing measurements over these sites to comprehensively analyze the dynamic and thermodynamic characteristics associated with cloud layers to reveal their differences between cloud-free and cloudy sky conditions, especially their physical mechanisms, feedbacks, turbulence features and thermodynamic structures. Finally, model simulations with detailed aerosol–cloud microphysical interactions are necessary to improve cloud parameterizations in climate models and to understand the cloud formation process and life cycle of clouds, as well as their mixing with the environment.

Acknowledgements. The data employed in this study were made available by the ARM program sponsored by the U.S. DOE. Special thanks are extended to Prof. Zhanqing LI and Prof. Yuejian XUAN for their contributions to the ARM AMF campaign at Shouxian. We would also like to thank all the other participants in the AMF-China experiment. This work was supported by the National Natural Science Foundation of China (Grant Nos. 40975001 and 61327810) and the Special Fund for Public Welfare Industry (Meteorology) (Grant No. GYHY201106046). WCW acknowledges the support of a grant (to SUNYA) from the Office of Science (BER), U.S. DOE and the Key National Basic Research Program on Global Change (Grant No. 2013CB955803).

REFERENCES

Bouniol, D., F. Couvreux, P. H. Kamsu-Tamo, M. Leplay, F. Guichard, F. Favot, and E. J. O'Connor, 2012: Diurnal and seasonal cycles of cloud occurrences, types, and radiative impact over West Africa. *J. Appl. Meteor. Climatol.*, **51**, 534–553, doi: 10.1175/JAMC-D-11-051.1.

Chen, C., and W. R. Cotton, 1987: The physics of the marine stratocumulus-capped mixed layer. *J. Atmos. Sci.*, **44**, 2951–2977.

Chernykh, I. V., and R. E. Eskridge, 1996: Determination of cloud amount and level from radiosonde soundings. *J. Appl. Meteor.*, **35**, 1362–1369.

Chernykh, I. V., O. A. Alduchov, and R. E. Eskridge, 2000: Trends in low and high cloud boundaries and errors in height determination of cloud boundaries. *Bull. Amer. Meteor. Soc.*, **82**, 1941–1947.

Clothiaux, E. E., T. P. Ackerman, G. C. Mace, K. P. Moran, R. T. Marchand, M. A. Miller, and B. E. Martner, 2000: Objective determination of cloud heights and radar reflectivities using a combination of active remote sensors at the ARM CART sites. *J. Appl. Meteor.*, **39**, 645–665.

Cotton, W. R., and R. A. Anthes, 1989: *Storm and Cloud Dynamics*. Academic Press, San Diego, USA, 883 pp.

Craven, J. P., R. E. Jewell, and H. E. Brooks, 2002: Comparison between observed convective cloud-base heights and lifting condensation level for two different lifted parcels. *Wea. Forecasting*, **17**, 885–890.

Del Genio, A. D., A. B. Wolf, and M. S. Yao, 2005: Evaluation of regional cloud feedbacks using single-column models. *J. Geophys. Res.*, **110**, D15S13, doi: 10.1029/2004JD005011.

Doswell III, C. A., and E. N. Rasmussen, 1994: The effect of neglecting the virtual temperature correction on CAPE calculations. *Wea. Forecasting*, **9**, 625–629.

Espy, J. P., 1841: *The Philosophy of Storms*. C. C. Little and J. Brown, Boston, USA, 552 pp.

Fan, X. H., H. B. Chen, X. G. Xia, Z. Q. Li, and M. Cribb, 2010: Aerosol optical properties from the Atmospheric Radiation Measurement Mobile Facility at Shouxian, China. *J. Geophys. Res.*, **115**, D00K33, doi: 10.1029/2010JD014650.

Haeffelin, M., and Coauthors, 2005: SIRTA, a ground-based atmospheric observatory for cloud and aerosol research. *Ann. Geophys.*, **23**, 253–275.

Illingworth, A. J., and Coauthors, 2007: Cloudnet–continuous evaluation of cloud profiles in seven operational models using ground-based observations. *Bull. Amer. Meteor. Soc.*, **88**, 883–898, doi: 10.1175/BAMS-88-6-883.

Intergovernmental Panel on Climate Change (IPCC), 2007: *The Physical Science Basis*. S. Solomon et al., Eds. Cambridge Univ. Press, Cambridge, U. K., 996 pp.

Intergovernmental Panel on Climate Change (IPCC), 2013: *The Physical Science Basis. Working Group I Contribution to the Fifth Assessment Report of the Intergovernmental Panel on Climate Change, Summary for Policymakers*. Stocker et al., Eds., 33 pp. [Available online at http://www.climatechange 2013.org/.]

Kalesse, H., and P. Kollias, 2013: Climatology of high cloud dynamics using profiling ARM Doppler radar observations. *J. Climate*, **26**, 6340–6359.

Kollias, P., M. A. Miller, K. L. Johnson, M. P. Jensen, and D. T. Troyan, 2009: Cloud, thermodynamic, and precipitation in West Africa during 2006. *J. Geophys. Res.*, **114**, D00E08, doi: 10.1029/2008JD010641.

Kunnen, R. P. J., C. Siewert, M. Meinke, W. Schröder, and K. D. Beheng, 2013: Numerically determined geometric collision kernels in spatially evolving isotropic turbulence relevant for droplets in clouds. *Atmospheric Research*, **127**, 8–21.

Li, Z. Q., M. Cribb, F. L. Chang, A. Trishchenko, and Y. Luo, 2005: Natural variability and sampling errors in solar radiation measurements for model validation over the Atmospheric Radiation Measurement Southern Great Plains region. *J. Geophys. Res.*, **110**, D15S19, doi: 10.1029/2004JD005028.

Li, Z. Q., and Coauthors, 2011: East Asian studies of tropospheric aerosols and their impact on regional climate (EAST-AIRC): An overview. *J. Geophys. Res.*, **116**, D00K34, doi: 10.1029/2010JD015257.

Mace, G. G., and S. Benson, 2008: The vertical structure of cloud occurrence and radiative forcing at the SGP ARM site as re-

vealed by 8 years of continuous data. *J. Climate*, **21**, 2591–2610, doi: 10.1175/2007JCLI1987.1.

Manzato, A., 2007. Sounding-derived indices for neural network based short-term thunderstorm and rainfall forecasts. *Atmospheric Research*, **83**, 349–365.

Minnis, P., Y. H. Yi, J. P. Huang, and J. K. Ayers, 2005: Relationships between radiosonde and RUC-2 meteorological conditions and cloud occurrence determined from ARM data. *J. Geophys. Res.*, **110**, D23, doi: 10.1029/2005JD006005.

Naud, C., J. P. Muller, and E. E. Clothiaux, 2003: Comparison between active sensor and radiosonde cloud boundaries over the ARM Southern Great Plains site. *J. Geophys. Res.*, **108**, D44140, doi: 10.1029/2002JD002887.

Poore, K. D., J. H. Wang, and W. B. Rossow, 1995: Cloud layer thicknesses from a combination of surface and upper-air observations. *J. Climate*, **8**, 550–568.

Protat, A., and Coauthors, 2014: Reconciling ground-based and space-based estimates of the frequency of occurrence and radiative effect of clouds around Darwin, Australia. *J. Appl. Meteor. Climatol.*, **53**, 456–478, doi: 10.1175/JAMC-D-13-072.1.

Rickenbach, T., R. Nieto Ferreira, N. Guy, and E. Williams, 2009: Radar-observed squall line propagation and the diurnal cycle of convection in Niamey, Niger, during the 2006 African Monsoon and Multidisciplinary Analysis Intensive Observing Period. *J. Geophys. Res.*, **114**, D03107, doi: 10.1029/2008JD010871.

Riihimaki, L. D., S. A. McFarlane, and J. M. Comstock, 2012: Climatology and formation of tropical midlevel clouds at the Darwin ARM Site. *J. Climate*, **25**, 6835–6850, doi: 10.1175/JCLI-D-11-00599.1.

Sassen, K., and Z. E. Wang, 2012: The clouds of the middle troposphere: composition, radiative impact, and global distribution. *Surveys in Geophysics*, **33**, 677–691, doi: 10.1007/s10712-011-9163-x.

Sherwood, S. C., S. Bony, and J. L. Dufresne, 2014: Spread in model climate sensitivity traced to atmospheric convective mixing. *Nature*, **505**, 37–42, doi: 10.1038/nature12829.

Sobel, A. H., S. E. Yuter, C. S. Bretherton, and G. N. Kiladis, 2004: Large-scale meteorology and deep convection during TRMM KWAJEX. *Mon. Wea. Rev.*, **132**, 422–444.

Stephens, G. L., 2005: Cloud feedbacks in the climate system: A critical review. *J. Climate*, **18**, 237–273.

Tao, W. K., J. P. Chen, Z. Q. Li, C. Wang, and C. D. Zhang, 2012: Impact of aerosols on convective clouds and precipitation. *Rev. Geophys.*, **50**, RG2001, doi: 10.1029/2011RG000369.

Trenberth, K., J. T. Fasullo, and J. Kiehl, 2009: Earth's global energy budget. *Bull. Amer. Meteor. Soc.*, **90**, 311–324, doi: 10.1175/2008BAMS2634.1.

Wang, J. H., and W. B. Rossow, 1995: Determination of cloud vertical structure from upper-air observations. *J. Appl. Meteor.*, **34**, 2243–2258.

Wang, J. H., W. B. Rossow, T. Uttal, and M. Rozendaal, 1999: Variability of cloud vertical structure during ASTEX observed from a combination of rawinsonde, radar, ceilometer, and satellite. *Mon. Wea. Rev.*, **127**, 2482–2502.

Wang, J. H., W. B. Rossow, and Y. C. Zhang, 2000: Cloud vertical structure and its variations from a 20-year global rawinsonde dataset. *J. Climate*, **13**, 3041–3056.

Xi, B. K., X. Q. Dong, P. Minnis, and M. M. Khaiyer, 2010: A 10 year climatology of cloud fraction and vertical distribution derived from both surface and GOES observations over the DOE ARM SGP Site. *J. Geophys. Res.*, **115**, D12, doi: 10.1029/2009JD012800.

Zhang, J. Q., H. B. Chen, Z. Q. Li, X. H. Fan, L. Peng, Y. Yu, and M. Cribb, 2010: Analysis of cloud layer structure in Shouxian, China using RS92 radiosonde aided by 95 GHz cloud radar. *J. Geophys. Res.*, **115**, D7, doi: 10.1029/2010JD014030.

Zhang, J. Q., Z. Q. Li, H. B. Chen, and M. Cribb, 2013: Validation of a radiosonde-based cloud layer detection method against a ground-based remote sensing method at multiple ARM sites. *J. Geophys. Res.*, **118**, 846–858, doi: 10.1029/2012JD018515.

Zhang, J. Q., Z. Q. Li, H. B. Chen, H. Yoo, and M. Cribb, 2014: Cloud vertical distribution from radiosonde, remote sensing, and model simulations. *Climate Dyn.*, **43**, 1129–1140, doi: 10.1007/s00382–014-2142-4.

Zhang, M. H., and Coauthors, 2005: Comparing clouds and their seasonal variations in 10 atmospheric general circulation models with satellite measurements. *J. Geophys. Res.*, **110**, D15, doi: 10.1029/2004JD005021.

Zhang, Y. Y., and S. A. Klein, 2010: Mechanisms affecting the transition from shallow to deep convection over land: Inferences from observations of the diurnal cycle collected at the ARM Southern Great Plains site. *J. Atmos. Sci.*, **67**, 2943–2959.

Zhao, C., and Coauthors, 2011: ARM Cloud Retrieval Ensemble Data Set (ACRED). DOE ARM technical report, DOE/SC-ARM-TR-099, Dep. of Energy, Washington, D. C., 28 pp. [Available online at http://www.arm.gov/publications/tech_reports/doe-sc-arm-tr-099.pdf.]

Zhao, C. F., and Coauthors, 2012: Toward understanding of differences in current cloud retrievals of ARM ground-based measurements. *J. Geophys. Res.*, **117**, D10206, doi: 10.1029/2011JD016792.

Zhao, C. F., Y. Z. Wang, Q. Q. Wang, Z. Q. Li, Z. E. Wang, and D. Liu, 2014: A new cloud and aerosol layer detection method based on micropulse lidar measurements. *J. Geophy. Res.*, **119**, 6788–6802, doi: 10.1002/2014JD021760.